Journal of Zhejiang University-SCIENCE A (Applied Physics & Engineering)
ISSN 1673-565X (Print); ISSN 1862-1775 (Online)
www.jzus.zju.edu.cn; link.springer.com
E-mail: jzus_a@zju.edu.cn

Adaptive robust control of soft bending actuators: an empirical nonlinear model-based approach*

Cong CHEN, Jun ZOU†‡

State Key Laboratory of Fluid Power and Mechatronic Systems, Zhejiang University, Hangzhou 310027, China

†E-mail: junzou@zju.edu.cn

Received Feb. 11, 2021; Revision accepted Apr. 21, 2021; Crosschecked Aug. 24, 2021

Abstract: Soft robotics, compared with their rigid counterparts, are able to adapt to uncharted environments, are superior in safe human-robot interactions, and have low cost, owing to the native compliance of the soft materials. However, customized complex structures, as well as the nonlinear and viscoelastic soft materials, pose a great challenge to accurate modeling and control of soft robotics, and impose restrictions on further applications. In this study, a unified modeling strategy is proposed to establish a complete dynamic model of the most widely used pneumatic soft bending actuator. First, a novel empirical nonlinear model with parametric and nonlinear uncertainties is identified to describe the nonlinear behaviors of pneumatic soft bending actuators. Second, an inner pressure dynamic model of a pneumatic soft bending actuator is established by introducing a modified valve flow rate model of the unbalanced pneumatic proportional valves. Third, an adaptive robust controller is designed using a backstepping method to handle and update the nonlinear and uncertain system. Finally, the experimental results of comparative trajectory tracking control indicate the validity of the proposed modeling and control method.

Key words: Pneumatic soft bending actuator; Empirical nonlinear model identification; Unbalanced pneumatic proportional valve modeling; Adaptive robust control; Trajectory tracking

https://doi.org/10.1631/jzus.A2100076 **CLC number:** TP242.3

1 Introduction

Soft robotics, which are made of soft elastomeric materials, have inspired a new wave of robotics (Kim et al., 2013) and attracted a great deal of attention in the past decade. Unlike conventional rigid industrial robots which can perform fast, precise, strong, and repetitive position control tasks, soft robotics are superior in human-robot interaction and can adapt to uncharted environments at potentially low cost (Laschi et al., 2016; Marchese et al., 2016; Yang et al., 2018) owing to the native compliance brought about by their soft materials (Hamidi et al., 2019). Numerous studies have focused on structural design, manufacturing, sensing, modeling, and control. As a result, many soft robotics which can perform motions including bending, twisting, stretching, and rotation have been developed (Blumenschein et al., 2018; Zhang et al., 2019).

Various methods are used to drive soft robotics. A fluid-driven method has been widely applied, thanks to its properties of excellent deformability and output force, high power-to-weight ratio, and low manufacturing cost (Zhang et al., 2021). However, the combination of nonlinear and viscoelastic soft materials leads to the obvious nonlinear behavior of soft robotics. Moreover, the nonlinear dynamics of the fluid-driven system and a customized complex structure make it difficult to gain accurate control of fluid-driven soft robotics (Polygerinos et al., 2017; Boyraz et al., 2018). Open-loop control is applied to

‡ Corresponding author

* Project supported by the National Natural Science Foundation of China (Nos. 51875507, 51821093, and U1908228)

ORCID: Cong CHEN, https://orcid.org/0000-0001-9510-0319; Jun ZOU, https://orcid.org/0000-0003-2443-3516

most fluid-driven soft robotics (Katzschmann, 2018), and a uniform closed-loop control framework is still lacking (Thuruthel et al., 2018).

As a compromise, low-level closed-loop control was developed to simplify the control duty by ignoring the ambiguous dynamics of soft robotics. Thus, the pressure (Ibrahim et al., 2019) or fluid mass (Deimel et al., 2016) of the inner chamber was dynamically controlled, rather than the position. This strategy of considering only the more definite air dynamics was more amenable to controller design. The position can be regulated indirectly when introducing the feedforward term of position-pressure mapping (Zhou et al., 2019; Fan et al., 2020), but control performance cannot be guaranteed. In contrast, high-level closed-loop control implements the position (or force) closed-loop control directly and is much more extensively applied to soft robotics.

Despite the difficulties, a number of studies have attempted to develop a theoretical model of high-level closed-loop control. Based on the incompressible Neo-Hookean (NH) material model, a quasi-static model (Polygerinos et al., 2015) was derived for a fiber-reinforced soft bending actuator (FRSBA) (Deimel and Brock, 2013) and used as an angle filter. Using the finite element method (FEM), the forward kinematic model (FKM) and inverse kinematic model (IKM) were analyzed by real-time numerical integration and designed a state estimator (Bieze et al., 2018). Using a rigid-link dynamic model of a soft continuum manipulator, Franco and Garriga-Casanovas (2021) derived an energy-shaping control law and a disturbance compensator. Using an analogical modeling method, a hybrid controller was introduced by Hyatt et al. (2019a). The outer loop was a feedforward term of inverse kinematic (IK) combining a proportional-differential (PD) controller using numerical IK, and the inner loop was a model predictive controller. Based on the constant curvature assumption and concentrated mass model, Falkenhahn et al. (2017) established a dynamic model for a bionic handling assistant using the Euler-Lagrange method, then a cascade controller using feedback linearization. A similar approach was adopted by Müller et al. (2020) to control the trajectory of a continuum manipulator. These studies explored the feasibility of using conventional mathematical model-based approaches to design controllers for fluid-driven soft robotics. The theoretical models above have the problems of high cost and low accuracy, which make suitable controllers difficult to design.

Considering the drawbacks of theoretical model-based approaches, pragmatic data-driven control methods have been widely used. Some studies adopted model-free tuning or training strategies. The proportional-integral-differential (PID) algorithm was widely adopted to control inflatable artificial muscles (Kwon et al., 2020). Furthermore, the tuning strategies and the roles of PID variants for pneumatic soft robotics were discussed. Khan et al. (2020) suggested that a PID controller essentially reduces to a proportional-integral (PI) controller. A PI controller was adopted to control flexible fluid actuators (FFAs) (Gerboni et al., 2017). Moreover, neural network (NN) controllers (Al-Ibadi et al., 2018; Pang et al., 2018) were also used to train the behavior of pneumatic soft robotics. These studies adopted a relatively simple approach to control fluid-driven soft robotics. However, these approaches were not amenable to model-based controller design (Bruder et al., 2019), and their stability and convergence were hard to prove. Several researchers attempted to derive empirical models from measured datasets and use them to design controllers. Training approaches were applied also to establishing empirical models for model-based controller design. Using the gradients of NN, a state-space model was established and used to design a model predictive controller (MPC) (Hyatt et al., 2019b). The weight matrices of an NN were also used to model the nonlinear dynamic process of a soft gripper. A model predictive neural controller (MPNC) was then designed (Luo et al., 2019). Using Gaussian process regulation (GPR), Jung et al. (2020) established a model of a soft pneumatic actuator, and after a simple conversion of the model, designed a sliding mode controller. In contrast, a lumped linear second-order model was found to be more explicit and was more widely applied. Using this data-driven linear model, an iterative sliding mode controller was introduced (Skorina et al., 2015). However, a linear model was not sufficient to consider the nonlinear behavior of soft robotics. By synthesizing the nonlinearities into parametric uncertainties, a robust backstepping controller was designed (Wang et al., 2018). The strategy of considering the unmodeled nonlinearities as perturbations was also adopted, and then an integral sliding mode controller was

designed (Khan and Li, 2020). A hysteresis model established by the Prandtl–Ishlinskii (P-I) method was also introduced. The model was used to design a feedforward hysteresis compensator that was added to a cascade controller (Abbasi et al., 2020). Using the strategy of fitting the parameters of the linear model as linear functions of pressure and synthesizing the parametric variations into model uncertainties, a sliding mode controller was designed after simplifying the high-order items of pressure (Chen et al., 2019). The Koopman operator was also used to identify a dynamic model of soft robotics. Based on this Koopman model, Bruder et al. (2019) designed an MPC controller. These empirical models made model-based controller design realizable, and stability analysis and convergence proofs were also possible. However, the obtained models cannot update online when implemented in real-time control, and therefore have limited scope for application. To solve this problem, online-updating models using adaptive Kalman filters (Li et al., 2018) or GPR (Tang et al., 2020) were proposed. Using the online-updating model, the application scope can be extended, but model validation is difficult and control performance cannot be guaranteed, especially when the model structure is inappropriate or when there are unmodeled uncertainties. Combining the idea of an offline empirical model and online-updating, the local GPR inverse model of a soft manipulator was updated (Fang et al., 2019), but the obtained model was a kind of quasi-static model and the dynamics of the robot pneumatic actuator unit were neglected. In our previous work (Chen et al., 2020), a complete model with bounded parametric uncertainties was established to describe nonlinear FRSBA dynamics and a nonlinear pneumatic system. An adaptive robust controller was then proposed to govern the nonlinear and uncertain system and update the model parameters.

In this paper, a novel model structure is first introduced for the most widely used FRSBA. By considering the model parameters of the linear model as functions of FRSBA position, an empirical nonlinear model is proposed to improve the model accuracy. The bounded parametric uncertainties and the modeling error are also analyzed. Next, a modified valve model is established to describe the flow rate of unbalanced pneumatic proportional valves. An adaptive robust algorithm is proposed to govern the nonlinear and uncertain system and update the model parameters while ensuring satisfactory control performance. Finally, the effectiveness of the improved modeling strategy and the validity of the designed controller are demonstrated through the experimental results of comparative trajectory tracking control.

2 Control system modeling

A schematic of the investigated system is given in Fig. 1. The pressure of the pneumatic supply is regulated by an LRPS pressure regulator (Festo, Germany). Two MD Pro pneumatic proportional valves (Parker Hannifin, USA) are used to govern the mass flow rates of the charging and exhaust air lines, respectively. Two SPAN pressure sensors (Festo) are used to measure the pressures of the regulated air source and FRSBA inner chamber. The FRSBA is installed vertically, and a WT931 inclinometer (Wit-Motion, China) mounted on the tip is used to measure the bending angle. The deformed shapes and corresponding bending angles under different inner chamber pressures can be seen in Fig. 5. The control algorithm was implemented with LabVIEW software and a CompactRIO-9047 controller (National Instruments, USA).

2.1 Empirical nonlinear dynamic model identification

The dynamics of the investigated FRSBA can be regarded as a single-input single-output (SISO) system, in which the input is the inner pressure P_v and the output is the bending angle y of the FRSBA. Considering the high performance-price ratio of the empirical model-based control method, the FRSBA model identification is implemented. With the pressure tracking controller designed in the controller design section (step 2), the inner pressure P_v can achieve good tracking performance for the [0, 1] Hz and [0, 0.5] Hz multi-sine excitation pressure trajectory P_{vd} designed in our previous work (Chen et al., 2020) (Figs. 2a and 2b). In these two experiments, the time series of the inner pressure as well the FRSBA bending angle were saved, thus the real excitation input and the response output were obtained. The time series obtained in the [0, 1] Hz pressure trajectory tracking control was then divided into two segments (Data1 and Data2) for system identification

and model validation, respectively. Using the time series (Data3) obtained in the [0, 0.5] Hz pressure trajectory tracking control, the identified model was further validated.

In previous studies, the following linear second-order transfer function was widely used to describe the nonlinear behavior of soft bending actuators (Skorina et al., 2015; Wang et al., 2018; Khan and Li, 2020):

$$\frac{Y(s)}{P_v(s)}=\frac{b}{s^2+cs+a}, \tag{1}$$

where $Y(s)$ is the Laplace transform of position function $y(t)$, s is the Laplace operator, t is the time variable, and a, b, and c are constant parameters.

This model simplifies the controller design, but leads to relatively inferior model accuracy, and control performance is also degraded. In actual application, the model parameters are found to vary with bending angle y, such that the following empirical nonlinear dynamic model is proposed to describe the FRSBA dynamics:

$$\ddot{y}(t)+c(y)\dot{y}(t)+a(y)y(t)=b(y)P_v+d+\Delta_1, \tag{2}$$

where $a(y)$, $b(y)$, and $c(y)$ are the model parameters varying with bending angle y, and $(d+\Delta_1)$ is the lumped modeling error, including external disturbance and terms like the initial deformation and unmodeled uncertainties. Specifically, d is the constant

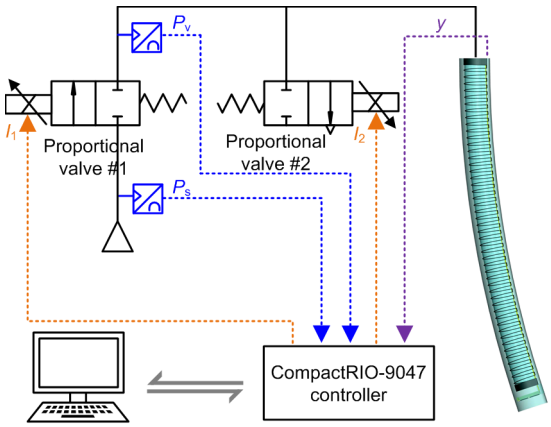

Fig. 1 Schematic of pneumatic soft bending actuator control system

I_1 and I_2 are the control currents of proportional valves #1 and #2, respectively; P_s is the source pressure

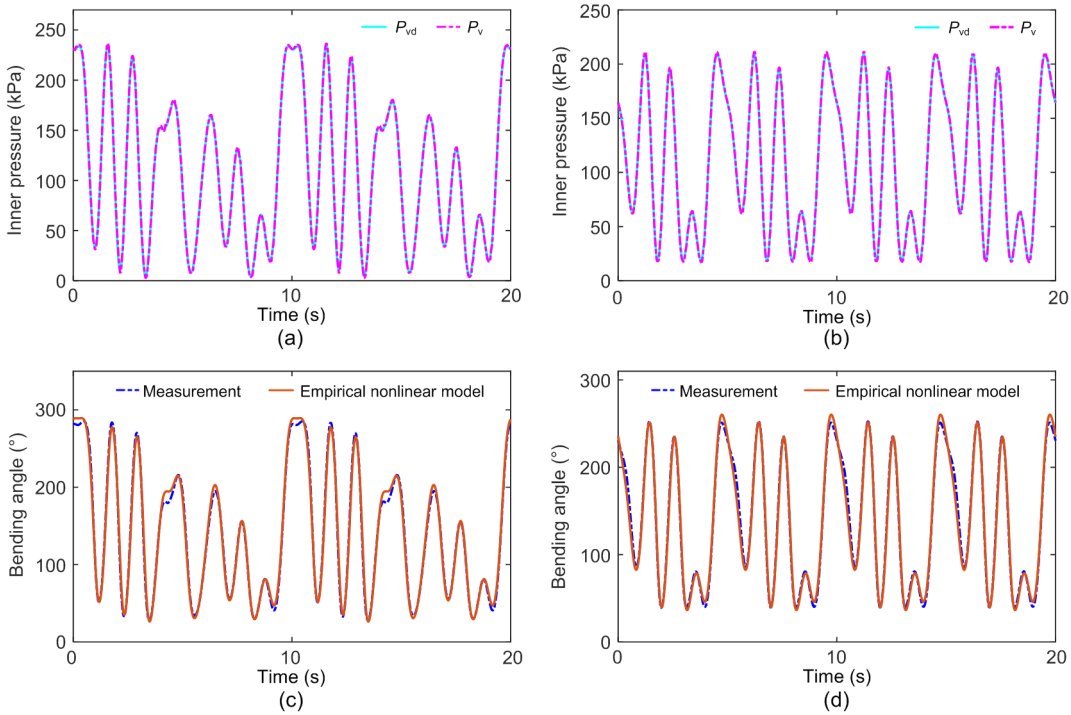

Fig. 2 Experimental results of pressure trajectory tracking and mode validation

(a) Pressure trajectory result of Data1; (b) Pressure trajectory result of Data3; (c) Model validation with Data2; (d) Model validation with Data3

component and Δ_1 is the time-varying component. The terms $a(y)$, $b(y)$, and $c(y)$ can be expanded in the following Taylor series:

$$a(y)=\sum_{i=0}^{m}a_i y^i(t), \tag{3}$$

$$b(y)=\sum_{j=0}^{n}b_j y^j(t), \tag{4}$$

$$c(y)=\sum_{k=0}^{r}c_k y^k(t), \tag{5}$$

where m, n, and r are the corresponding orders of the Taylor series to be determined, and a_i, b_j, and c_k are the corresponding coefficients to be identified.

Introducing a stable low-pass filter $H_f(s)$ that has a relative degree of not less than two and applying the filter to Eqs. (2)–(5), under the assumption that $\Delta_1=0$, we can obtain

$$\begin{aligned}\ddot{y}_f=&\sum_{i=0}^{m}a_i\left(-y^{i+1}\right)_f+\sum_{j=0}^{n}b_j\left(y^jP_v\right)_f\\&+\sum_{k=0}^{r}c_k\left(-y^k\dot{y}\right)_f+d(1)_f,\end{aligned} \tag{6}$$

where $\ddot{y}_f$ is the output of filter $s^2H_f(s)$ for the input y; $\left(-y^k\dot{y}\right)_f$ is the output of filter $sH_f(s)$ for input $\left(-\dfrac{y^{k+1}}{k+1}\right)$; $(-y^{i+1})_f$, $(y^jP_v)_f$, and $(1)_f$ are the outputs of filter $H_f(s)$ for the inputs $-y^{i+1}$, y^jP_v, and 1, respectively. Defining the following regressor, parameter vector, and output vector:

$$\boldsymbol{Y}=\ddot{y}_f, \tag{7}$$

$$\begin{aligned}\boldsymbol{\Phi}=\big[&(-y)_f,\cdots,\left(-y^{m+1}\right)_f,\left(y^0P_v\right)_f,\cdots,\\&\left(y^nP_v\right)_f,\left(-y^0\dot{y}\right)_f,\cdots,\left(-y^l\dot{y}\right)_f,(1)_f\big]^{\mathrm{T}},\end{aligned} \tag{8}$$

$$\boldsymbol{\theta}_{\mathrm{FRSBA}}=\left[a_0,\cdots,a_m,b_0,\cdots,b_n,c_0,\cdots,c_l,d\right]^{\mathrm{T}}, \tag{9}$$

a linear regression model can be obtained by

$$\boldsymbol{Y}=\boldsymbol{\Phi}^{\mathrm{T}}\boldsymbol{\theta}_{\mathrm{FRSBA}}. \tag{10}$$

Weighting the output fitting accuracy against the model complexity, the orders of the Taylor series are set to be m=2, n=0, and r=3. By least square (LS) parameter estimation, the mean values and confidence intervals of $\boldsymbol{\theta}_{\mathrm{FRSBA}}$ can be obtained.

With the mean parameter values given in Table 1, the proposed empirical nonlinear model was validated (Figs. 2c and 2d). The normalized root mean square error (NRMSE) fitness values were 92.8772% for Data2 and 90.8123% for Data3. Note that there are still some distinctions between the measurement output and the model output. Therefore, it is necessary to estimate a reasonable parameter bound, and three standard deviations of the means given in Table 1 were adopted.

Table 1 Identified parameters of the empirical nonlinear model

Parameter	Mean	Confidence interval
a_0	89.9733	[87.8895, 92.0572]
a_1	−0.1875	[−0.2015, −0.1736]
a_2	2.8943×10^{-4}	[2.6020×10^{-4}, 3.1866×10^{-4}]
b_0	64.3797	[63.8050, 64.9543]
c_0	15.4547	[14.8738, 16.0355]
c_1	-6.9640×10^{-2}	[-8.3345×10^{-2}, -5.5935×10^{-2}]
c_2	8.0505×10^{-5}	[1.5434×10^{-5}, 1.4558×10^{-4}]
c_3	5.0667×10^{-7}	[2.9380×10^{-7}, 7.1955×10^{-7}]
d	2277.8173	[2204.9646, 2350.6701]

2.2 Pneumatic system modeling

The dynamics of the air inside the FRSBA chamber is regarded as an isothermal process during deformation. Considering that the deformation of a FRSBA is restricted by soft inextensible fiber and fabric, the volume V of the inner chamber can be regarded as a bounded parameter. Then, the dynamics of P_v can be obtained by calculating the derivative of the ideal gas law:

$$\dot{P}_v=\frac{RT}{S_pV}(Q_{m1}-Q_{m2}-Q_{ml})+\Delta_2, \tag{11}$$

where the ideal gas constant R=287 N·m/(kg·K); T is the thermodynamic temperature; S_p=1000 is a coefficient; Q_{m1}, Q_{m2}, and Q_{ml} are the mass flow rates of the air charging, exhaust, and leakage, respectively; Δ_2 is the model error.

The mass flow rates regulated by pneumatic proportional valves are related to the valves' orifice area A_v (Finnemore and Franzini, 2002), by

$$Q_{\mathrm{me}}\left(P_{\mathrm{u}}, P_{\mathrm{d}}\right)= \begin{cases} C_{\mathrm{f}} A_{\mathrm{v}} C_{1} \dfrac{P_{\mathrm{u}}}{\sqrt{T}}, & \dfrac{P_{\mathrm{d}}}{P_{\mathrm{u}}} \leq 0.528, \\ C_{\mathrm{f}} A_{\mathrm{v}} C_{2} \dfrac{P_{\mathrm{u}}}{\sqrt{T}}\left(\dfrac{P_{\mathrm{d}}}{P_{\mathrm{u}}}\right)^{\frac{1}{\kappa}} \sqrt{1-\left(\dfrac{P_{\mathrm{d}}}{P_{\mathrm{u}}}\right)^{\frac{\kappa-1}{\kappa}}}, & \dfrac{P_{\mathrm{d}}}{P_{\mathrm{u}}} > 0.528, \end{cases} \tag{12}$$

where P_{u} and P_{d} are the upstream and downstream pressures, and C_{f}, κ=1.4, $C_{1}=\sqrt{\dfrac{\kappa}{R}\left(\dfrac{2}{\kappa+1}\right)^{\frac{\kappa-1}{\kappa+1}}}$, and $C_{2}=\sqrt{\dfrac{2\kappa}{R(\kappa+1)}}$ are coefficients.

As can be seen in Fig. 3, the orifice area A_{v} of the unbalanced pneumatic proportional valves is determined by the spool displacement x_{v}, the dynamics of which can be given by

$$F_{\mathrm{mag}}=m_{\mathrm{s}}\ddot{x}_{\mathrm{v}}+b_{\mathrm{s}}\dot{x}_{\mathrm{v}}+k_{\mathrm{s}}x_{\mathrm{v}}+F_{\mathrm{flu}}+F_{0}, \tag{13}$$

where $F_{\mathrm{mag}}=k_{\mathrm{i}}I$ is the electromagnetic force, k_{i} is the electromagnetic force coefficient, I is the control current, m_{s} is the spool mass, b_{s} is the dumping coefficient, k_{s} is the spring stiffness, F_0 is the initial spring force, and F_{flu} is the steady airflow force expressed as follows (Xiang, 2010):

$$F_{\mathrm{flu}}=\left(k_{\mathrm{f}1}-k_{\mathrm{f}2}\frac{x_{\mathrm{v}}}{x_{\mathrm{vmax}}}\right)\pi\left(P_{\mathrm{u}}r_{0}^{2}-P_{\mathrm{d}}r_{1}^{2}\right), \tag{14}$$

where $k_{\mathrm{f}1}$ and $k_{\mathrm{f}2}$ are correction factors; x_{vmax} is the maximum spool displacement; r_0 and r_1 are the outer and inner radii of valve seat, respectively. Without loss of generality, the valve dynamics are neglected and the spool displacement x_{v} is directly related to the control input I, upstream pressure P_{u}, and downstream pressure P_{d} by a known static mapping (Yao et al., 2000; Mohanty and Yao, 2011):

$$x_{\mathrm{v}}=\frac{k_{\mathrm{i}}I-k_{\mathrm{f}1}\pi\left(P_{\mathrm{u}}r_{0}^{2}-P_{\mathrm{d}}r_{1}^{2}\right)-F_{0}}{k_{\mathrm{s}}-\dfrac{k_{\mathrm{f}2}}{x_{\mathrm{vmax}}}\pi\left(P_{\mathrm{u}}r_{0}^{2}-P_{\mathrm{d}}r_{1}^{2}\right)}. \tag{15}$$

The valves' orifice area A_{v} related to control input I, upstream pressure P_{u}, and downstream pressure P_{d} can be expressed as

$$A_{\mathrm{v}}=2\pi r_{1}x_{\mathrm{v}}=\frac{k_{\mathrm{v}1}I-k_{\mathrm{v}3}P_{\mathrm{u}}+k_{\mathrm{v}5}P_{\mathrm{d}}-k_{\mathrm{v}6}}{1-k_{\mathrm{v}2}P_{\mathrm{u}}+k_{\mathrm{v}4}P_{\mathrm{d}}}, \tag{16}$$

where $k_{\mathrm{v}1}=\dfrac{2\pi r_{1}k_{\mathrm{i}}}{k_{\mathrm{s}}}$, $k_{\mathrm{v}2}=\dfrac{k_{\mathrm{f}2}\pi r_{0}^{2}}{\delta_{\mathrm{m}}k_{\mathrm{s}}}$, $k_{\mathrm{v}3}=\dfrac{2\pi r_{1}k_{\mathrm{f}1}\pi r_{0}^{2}}{k_{\mathrm{s}}}$, $k_{\mathrm{v}4}=\dfrac{k_{\mathrm{f}2}\pi r_{1}^{2}}{\delta_{\mathrm{m}}k_{\mathrm{s}}}$, $k_{\mathrm{v}5}=\dfrac{2\pi r_{1}k_{\mathrm{f}1}\pi r_{1}^{2}}{k_{\mathrm{s}}}$, and $k_{\mathrm{v}6}=\dfrac{2\pi r_{1}F_{0}}{k_{\mathrm{s}}}$ are coefficients to be fitted.

Substituting Eq. (12) into Eq. (8), the mass flow rates $Q_{\mathrm{m}1}$, $Q_{\mathrm{m}2}$, and Q_{ml} can be calculated as follows:

$$\begin{aligned} Q_{\mathrm{m}1}&=g_{2}\left(S_{\mathrm{P}}P_{\mathrm{s}}+P_{\mathrm{atm}}, S_{\mathrm{P}}P_{\mathrm{v}}+P_{\mathrm{atm}}\right) \\ &\times\left[g_{3}\left(S_{\mathrm{P}}P_{\mathrm{s}}, S_{\mathrm{P}}P_{\mathrm{v}}\right)\left(k_{\mathrm{v}1}I-k_{\mathrm{v}6}\right)+g_{4}\left(S_{\mathrm{P}}P_{\mathrm{s}}, S_{\mathrm{P}}P_{\mathrm{v}}\right)\right], \end{aligned} \tag{17}$$

$$\begin{aligned} Q_{\mathrm{m}2}&=g_{2}\left(S_{\mathrm{P}}P_{\mathrm{v}}+P_{\mathrm{atm}}, P_{\mathrm{atm}}\right) \\ &\times\left[g_{3}\left(S_{\mathrm{P}}P_{\mathrm{v}}, 0\right)\left(k_{\mathrm{v}1}I-k_{\mathrm{v}6}\right)+g_{4}\left(S_{\mathrm{P}}P_{\mathrm{v}}, 0\right)\right], \end{aligned} \tag{18}$$

$$Q_{\mathrm{ml}}=g_{2}\left(S_{\mathrm{P}}P_{\mathrm{v}}+P_{\mathrm{atm}}, P_{\mathrm{atm}}\right)A_{\mathrm{l}}, \tag{19}$$

where A_{l} is the equivalent orifice area of leakage, and P_{atm} is the standard atmosphere. $g_2(P_{\mathrm{u}}, P_{\mathrm{d}})$, $g_3(P_{\mathrm{u}}, P_{\mathrm{d}})$, and $g_4(P_{\mathrm{u}}, P_{\mathrm{d}})$ are known functions related to upstream pressure P_{u} and downstream pressure P_{d}.

$$g_{\mathrm{l}}=\frac{RT}{S_{\mathrm{p}}V}, \tag{20}$$

$$g_{2}\left(P_{\mathrm{u}}, P_{\mathrm{d}}\right)= \begin{cases} C_{\mathrm{f}}C_{1}\dfrac{P_{\mathrm{u}}}{\sqrt{T}}, & \dfrac{P_{\mathrm{d}}}{P_{\mathrm{u}}} \leq 0.528, \\ C_{\mathrm{f}}C_{2}\dfrac{P_{\mathrm{u}}}{\sqrt{T}}\left(\dfrac{P_{\mathrm{d}}}{P_{\mathrm{u}}}\right)^{\frac{1}{\kappa}}\sqrt{1-\left(\dfrac{P_{\mathrm{d}}}{P_{\mathrm{u}}}\right)^{\frac{\kappa-1}{\kappa}}}, & \dfrac{P_{\mathrm{d}}}{P_{\mathrm{u}}} > 0.528, \end{cases} \tag{21}$$

$$g_{3}\left(P_{\mathrm{u}}, P_{\mathrm{d}}\right)=\frac{1}{1-k_{\mathrm{v}2}P_{\mathrm{u}}+k_{\mathrm{v}4}P_{\mathrm{d}}}, \tag{22}$$

$$g_{4}\left(P_{\mathrm{u}}, P_{\mathrm{d}}\right)=\frac{-k_{\mathrm{v}3}P_{\mathrm{u}}+k_{\mathrm{v}5}P_{\mathrm{d}}}{1-k_{\mathrm{v}2}P_{\mathrm{u}}+k_{\mathrm{v}4}P_{\mathrm{d}}}. \tag{23}$$

With the mean values of $k_{\mathrm{v}1}$, $k_{\mathrm{v}2}$, $k_{\mathrm{v}3}$, $k_{\mathrm{v}4}$, $k_{\mathrm{v}5}$, and $k_{\mathrm{v}6}$ obtained by LS method, there is good agreement between the measured mass flow rate and the modified valve model (Fig. 4). Similarly, the confidence intervals of the parameters are also estimated

to cover the distinctions between the measured mass flow rates and the modified valve model. To reduce the complexity of controller design, only the variation regions of k_{v1} and k_{v6} are analyzed and regarded as bounded parametric uncertainties.

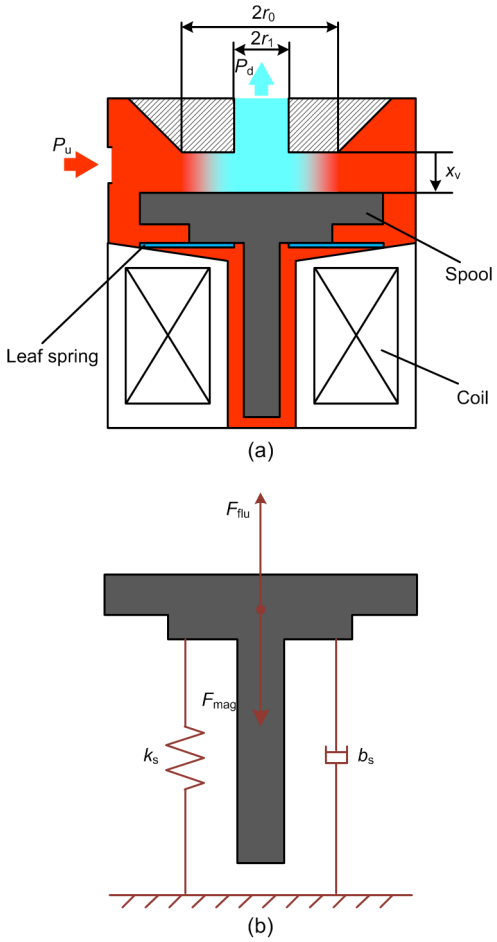

Fig. 3 Simple structure of the unbalance valve (a) and one-degree of freedom model of the spool (b)

2.3 Problem formulation

Separating the air charging and exhaust processes, the complete model of the investigated control system can be synthesized from Eqs. (2)–(5), (11), and (17)–(19), as follows:

$$\begin{cases}\dot{x}_1 = x_2, \\ \dot{x}_2 = \boldsymbol{\varphi}_a^{\mathrm{T}}\boldsymbol{\theta}_a + \theta_9 P_v + \Delta_1,\end{cases} \tag{24}$$

$$\dot{P}_v = f_1(\theta_{10} I_i - \theta_{11}) + f_2 - f_3\theta_{12} + \Delta_2, \quad i = 1, 2, \tag{25}$$

where the states are $\boldsymbol{x} = [x_1, x_2]^{\mathrm{T}} = [y, \dot{y}]^{\mathrm{T}}$ and $\boldsymbol{\varphi}_a = [-x_1, x_1^2, -x_1^3, -x_2, x_1x_2, -x_1^2x_2, -x_1^3x_2, 1]^{\mathrm{T}}$; the model parameters are $\boldsymbol{\theta}=[\theta_1, \theta_2, \theta_3, \theta_4, \theta_5, \theta_6, \theta_7, \theta_8, \theta_9, \theta_{10}, \theta_{11}, \theta_{12}]^{\mathrm{T}}=[a_0, -a_1, a_2, c_0, -c_1, c_2, c_3, d, b_0, k_{v1}, k_{v6}, A_1]^{\mathrm{T}}$ and $\boldsymbol{\theta}_a=[\theta_1, \theta_2, \theta_3, \theta_4, \theta_5, \theta_6, \theta_7, \theta_8]^{\mathrm{T}}$; i=1, 2 denotes the air charging and exhaust process, respectively; f_1, f_2, and f_3 are known items expressed as:

$$f_1 = \begin{cases} g_1 g_2(S_P P_s + P_{atm}, S_P P_v + P_{atm}) \times g_3(S_P P_s, S_P P_v), & i = 1, \\ -g_1 g_2(S_P P_v + P_{atm}, P_{atm}) \times g_3(S_P P_v, 0), & i = 2, \end{cases} \tag{26}$$

$$f_2 = \begin{cases} g_1 g_2(S_P P_s + P_{atm}, S_P P_v + P_{atm}) \times g_4(S_P P_s, S_P P_v), & i = 1, \\ -g_1 g_2(S_P P_v + P_{atm}, P_{atm}) \times g_4(S_P P_v, 0), & i = 2, \end{cases} \tag{27}$$

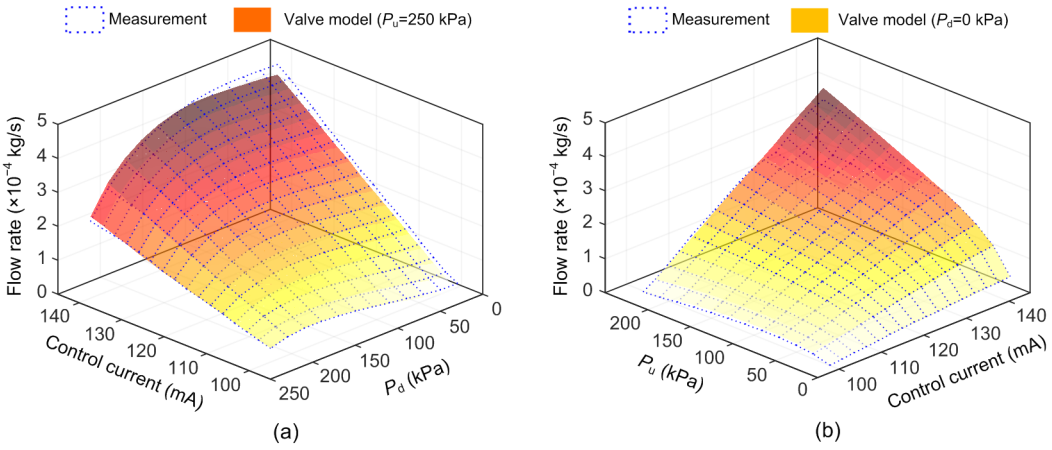

Fig. 4 Modified valve model validation under constant upstream pressure (a) and constant downstream pressure (b)

$$f_3 = g_1 g_2 \left(S_\mathrm{P} P_\mathrm{v} + P_\mathrm{atm}, P_\mathrm{atm} \right). \tag{28}$$

As mentioned above, the nominal values of model parameters $\boldsymbol{\theta}$ obtained from offline identification are the mean values of experimental measurements. In different conditions, model parameters $\boldsymbol{\theta}$ may vary within a determined parametric bound, as follows:

$$\hat{\boldsymbol{\theta}} \in \Omega_{\boldsymbol{\theta}} \triangleq \left\{ \boldsymbol{\theta} : \boldsymbol{\theta}_{\min} \le \boldsymbol{\theta} \le \boldsymbol{\theta}_{\max} \right\}, \tag{29}$$

where the lower bound $\boldsymbol{\theta}_{\min}=[\theta_{1\min}, \theta_{2\min}, \theta_{3\min}, \theta_{4\min}, \theta_{5\min}, \theta_{6\min}, \theta_{7\min}, \theta_{8\min}, \theta_{9\min}, \theta_{10\min}, \theta_{11\min}, \theta_{12\min}]^\mathrm{T}$ and the upper bound $\boldsymbol{\theta}_{\max}=[\theta_{1\max}, \theta_{2\max}, \theta_{3\max}, \theta_{4\max}, \theta_{5\max}, \theta_{6\max}, \theta_{7\max}, \theta_{8\max}, \theta_{9\max}, \theta_{10\max}, \theta_{11\max}, \theta_{12\max}]^\mathrm{T}$ are known.

3 Controller design

The controller structure shown in Fig. 5 consists of the following parts.

3.1 Discontinuous projection-based parameter adaptation

A discontinuous projection-based parameter adaptation is introduced to update the model parameters:

$$\dot{\hat{\boldsymbol{\theta}}} = \mathrm{Proj}_{\hat{\boldsymbol{\theta}}}(\boldsymbol{\Gamma}\boldsymbol{\tau}), \tag{30}$$

where $\boldsymbol{\Gamma}>0$ is a positive-definite diagonal matrix, and $\boldsymbol{\tau}$ is the adaptation function. $\mathrm{Proj}_{\hat{\boldsymbol{\theta}}}(\bullet_i)$ is the discontinuous projection mapping as

$$\mathrm{Proj}_{\hat{\boldsymbol{\theta}}}(\bullet_i) = \begin{cases} 0, & \text{if } \hat{\theta}_i = \theta_{i\max} \text{ and } \bullet_i > 0, \\ 0, & \text{if } \hat{\theta}_i = \theta_{i\min} \text{ and } \bullet_i < 0, \\ \bullet_i, & \text{otherwise}, \end{cases} \tag{31}$$

and $\hat{\boldsymbol{\theta}} = \left[\hat{\theta}_1, \hat{\theta}_2, \hat{\theta}_3, \hat{\theta}_4, \hat{\theta}_5, \hat{\theta}_6, \hat{\theta}_7, \hat{\theta}_8, \hat{\theta}_9, \hat{\theta}_{10}, \hat{\theta}_{11}, \hat{\theta}_{12} \right]^\mathrm{T}$ is the estimated value of $\boldsymbol{\theta}$. The resulting parameter estimation error can be given by $\tilde{\boldsymbol{\theta}} = \hat{\boldsymbol{\theta}} - \boldsymbol{\theta} = \left[\tilde{\theta}_1, \tilde{\theta}_2, \tilde{\theta}_3, \tilde{\theta}_4, \tilde{\theta}_5, \tilde{\theta}_6, \tilde{\theta}_7, \tilde{\theta}_8, \tilde{\theta}_9, \tilde{\theta}_{10}, \tilde{\theta}_{11}, \tilde{\theta}_{12} \right]^\mathrm{T}$.

Consequently, the discontinuous projection mapping formulated by Eq. (18) can guarantee the following properties for any $\boldsymbol{\tau}$ (Yao, 1997):

$$\begin{aligned} &\mathrm{P1}: \ \hat{\boldsymbol{\theta}} \in \Omega_{\boldsymbol{\theta}} \triangleq \left\{ \boldsymbol{\theta} : \boldsymbol{\theta}_{\min} \le \boldsymbol{\theta} \le \boldsymbol{\theta}_{\max} \right\}, \\ &\mathrm{P2}: \ \tilde{\boldsymbol{\theta}}^\mathrm{T} \left[\boldsymbol{\Gamma}^{-1} \mathrm{Proj}_{\hat{\boldsymbol{\theta}}}(\boldsymbol{\Gamma}\boldsymbol{\tau}) - \boldsymbol{\tau} \right] \le 0, \forall \boldsymbol{\tau}. \end{aligned} \tag{32}$$

3.2 Working mode design

The air charging and exhaust processes are separated using the working modes (Liu and Yao, 2008). Mode 1 and Mode 2 (Table 2) denote enabling only the charging valve and exhaust valve, respectively, while Mode 3 represents turning off both valves.

Table 2 Working mode design

$\dot{x}_\mathrm{d}$	x_1-x_d	Mode
>0	/	1
<0	/	2
=0	$>\varepsilon_0$	2
=0	$<-\varepsilon_0$	1
=0	Otherwise	3

$[x_\mathrm{d}, \dot{x}_\mathrm{d}]=[y_\mathrm{d}, \dot{y}_\mathrm{d}]$ are the position and velocity of the desired trajectory; ε_0 is the allowable tracking error

3.3 Controller design

To govern the system with nonlinearities and uncertainties, the following adaptive robust controller (ARC) was designed based on a backstepping method.

Step 1: Defining $e=x_1-x_\mathrm{d}$ as the bending angle tracking error, the following switching-function like quantity is given:

$$S_1 = \dot{e} + K_{\mathrm{S}1} e, \tag{33}$$

where $K_{\mathrm{S}1}>0$ is a positive feedback gain to be tuned. Accordingly, e will converge to zero as S_1 converges to zero.

From Eqs. (24) and (33), the dynamics can be obtained as follows:

$$\dot{S}_1 = \ddot{e} + K_{\mathrm{S}1}\dot{e} = \boldsymbol{\varphi}_\mathrm{a}^\mathrm{T}\boldsymbol{\theta}_\mathrm{a} + \theta_9 P_\mathrm{v} + \Delta_1 + w, \tag{34}$$

where $w = K_{\mathrm{S}1}\left(x_2 - \dot{x}_\mathrm{d}\right) - \ddot{x}_\mathrm{d}$ is a known item, and

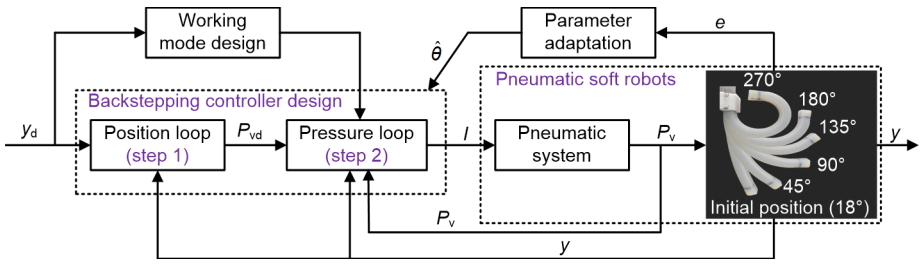

Fig. 5 Controller structure

the desired pressure input P_{vd} of Step 1 is designed as follows:

$$P_{\mathrm{vd}} = P_{\mathrm{vda}} + P_{\mathrm{vds1}} + P_{\mathrm{vds2}}, \tag{35}$$

$$P_{\mathrm{vda}} = \frac{1}{\hat{\theta}_9}\left(-\boldsymbol{\varphi}_{\mathrm{a}}^{\mathrm{T}}\hat{\boldsymbol{\theta}}_{\mathrm{a}} - w\right), \tag{36}$$

$$P_{\mathrm{vds1}} = -\frac{1}{\theta_{9\min}}K_1 S_1, \tag{37}$$

where $K_1>0$ is a feedback gain, and P_{vds2} is a nonlinear feedback function satisfying the following robust performance conditions:

$$\text{(i)}:\ S_1 P_{\mathrm{vds2}} \le 0,\quad \text{(ii)}:\ S_1\left[\theta_9 P_{\mathrm{vds2}} - \boldsymbol{\varphi}_{\mathrm{b}}^{\mathrm{T}}\tilde{\boldsymbol{\theta}}_{\mathrm{b}} + \Delta_1\right] \le \varepsilon_1, \tag{38}$$

where $\varepsilon_1>0$ is a design parameter that can be arbitrarily small; $\boldsymbol{\varphi}_{\mathrm{b}} = \left[\boldsymbol{\varphi}_{\mathrm{a}}^{\mathrm{T}}, P_{\mathrm{vda}}\right]^{\mathrm{T}}$, and $\tilde{\boldsymbol{\theta}}_{\mathrm{b}} = \left[\tilde{\boldsymbol{\theta}}_{\mathrm{a}}^{\mathrm{T}}, \tilde{\theta}_9\right]^{\mathrm{T}}$; the following adaptation function can be given:

$$\boldsymbol{\tau}_1 = \boldsymbol{\varphi}_{\mathrm{b}} S_1. \tag{39}$$

Defining a positive-definite function $V_1 = \frac{1}{2}S_1^2$ and the pressure input discrepancy $S_2 = P_{\mathrm{v}} - P_{\mathrm{vd}}$, we can derive that:

$$\begin{aligned}\dot{V}_1 = S_1\dot{S}_1 &= \frac{\theta_9}{\theta_{9\min}}\left(-K_1 S_1^2\right) + S_1\left[\theta_9 P_{\mathrm{vds2}} - \boldsymbol{\varphi}_{\mathrm{b}}^{\mathrm{T}}\tilde{\boldsymbol{\theta}}_{\mathrm{b}} + \Delta_1\right] \\ &+ \theta_9 S_1 S_2 \le \frac{\theta_9}{\theta_{9\min}}\left(-K_1 S_1^2\right) + \varepsilon_1 + \theta_9 S_1 S_2.\end{aligned} \tag{40}$$

Step 2: After designing the desired pressure input P_{vd} and separating the air charging (Mode 1, i=1) and exhaust (Mode 2, i=2) processes, the dynamics of pressure input discrepancy can be obtained from Eqs. (25) and (35)–(38), as follows:

$$\dot{S}_2 = f_1\left(\theta_{10} I_i - \theta_{11}\right) + f_2 - f_3\theta_{11} + \Delta_2 - \dot{P}_{\mathrm{vdc}} - \dot{P}_{\mathrm{vdu}}, \tag{41}$$

where $\dot{P}_{\mathrm{vdc}}$ and $\dot{P}_{\mathrm{vdu}}$ are the calculable and incalculable parts, respectively, as follows:

$$\dot{P}_{\mathrm{vdc}} = \frac{\partial P_{\mathrm{vd}}}{\partial x_1}x_2 + \frac{\partial P_{\mathrm{vd}}}{\partial x_2}\dot{\hat{x}}_2 + \frac{\partial P_{\mathrm{vd}}}{\partial t}, \tag{42}$$

$$\dot{P}_{\mathrm{vdu}} = \frac{\partial P_{\mathrm{vd}}}{\partial x_2}\left(\dot{x}_2 - \dot{\hat{x}}_2\right) + \frac{\partial P_{\mathrm{vd}}}{\partial \hat{\boldsymbol{\theta}}_{\mathrm{a}}}\dot{\hat{\boldsymbol{\theta}}}_{\mathrm{a}}. \tag{43}$$

Accordingly, the control input of step 2 is given by

$$I_i = I_{i\mathrm{a}} + I_{i\mathrm{s1}} + I_{i\mathrm{s2}}, \tag{44}$$

$$I_{i\mathrm{a}} = \frac{\hat{\theta}_{11}f_1 - f_2 + \hat{\theta}_{12}f_3 + \dot{P}_{\mathrm{vdc}} - \hat{\theta}_9 S_1}{\hat{\theta}_{10}f_1}, \tag{45}$$

$$I_{i\mathrm{s1}} = -\frac{1}{\theta_{10\min}f_1}K_2 S_2, \tag{46}$$

where $K_2>0$ is a feedback gain, and $I_{i\mathrm{s2}}$ is a nonlinear feedback function satisfying the following robust performance conditions:

$$\begin{aligned}&\text{(i)}:\ S_2 f_1 I_{i\mathrm{s2}} \le 0, \\ &\text{(ii)}:\ S_2\left[\theta_{10} f_1 I_{i\mathrm{s2}} - \boldsymbol{\varphi}_{\mathrm{c}}^{\mathrm{T}}\tilde{\boldsymbol{\theta}} + \left(\Delta_2 - \frac{\partial P_{\mathrm{vd}}}{\partial x_1}\Delta_1\right)\right] \le \varepsilon_2,\end{aligned} \tag{47}$$

where $\boldsymbol{\varphi}_{\mathrm{c}} = \left[-\frac{\partial P_{\mathrm{vd}}}{\partial x_2}\boldsymbol{\varphi}_{\mathrm{a}}^{\mathrm{T}}, S_1 - \frac{\partial P_{\mathrm{vd}}}{\partial x_2}P_{\mathrm{v}}, f_1 I_{i\mathrm{a}}, -f_1, -f_3\right]^{\mathrm{T}}$; $\varepsilon_2>0$ is a design parameter that can be arbitrarily

small. Then, the adaptation function is eventually obtained:

$$\boldsymbol{\tau}=\left[\boldsymbol{\tau}_1^{\mathrm{T}},\mathbf{0}\right]^{\mathrm{T}}+\boldsymbol{\varphi}_{\mathrm{c}}S_2. \tag{48}$$

Defining a positive-definite function $V_2=V_1+\frac{1}{2}S_2^2$, we can derive that:

$$\begin{aligned}V_2&\le\frac{\theta_9}{\theta_{9\min}}\left(-K_1S_1^2\right)+\varepsilon_1+\theta_9S_1S_2+\frac{\theta_{10}}{\theta_{10\min}}\left(-K_2S_2^2\right)\\&+S_2\left[\theta_{10}f_1I_{is2}-\boldsymbol{\varphi}_{\mathrm{c}}^{\mathrm{T}}\tilde{\boldsymbol{\theta}}+\left(\Delta_2-\frac{\partial P_{\mathrm{vd}}}{\partial x_1}\Delta_1\right)\right]-\theta_9S_1S_2\\&\le\frac{\theta_9}{\theta_{9\min}}\left(-K_1S_1^2\right)+\frac{\theta_{10}}{\theta_{10\min}}\left(-K_2S_2^2\right)+\varepsilon_1+\varepsilon_2\le-\lambda V_2+\varepsilon,\end{aligned} \tag{49}$$

where $\lambda=\min\{K_1, K_2\}$, and $\varepsilon=\varepsilon_1+\varepsilon_2$.

Therefore, the system is stable and the tracking error is bounded. Additionally, the transient and steady-state tracking error is quantified as

$$V_2\le V_2(0)\exp\left(-2\lambda t\right)+\frac{\varepsilon}{2\lambda}\left[1-\exp\left(-2\lambda t\right)\right]. \tag{50}$$

Assuming that the system subjects only to parametric uncertainties and defining a positive-definite function $V_3=V_2+\frac{1}{2}\tilde{\boldsymbol{\theta}}^{\mathrm{T}}\boldsymbol{\Gamma}^{-1}\tilde{\boldsymbol{\theta}}$, noting that $\dot{\tilde{\boldsymbol{\theta}}}=\dot{\hat{\boldsymbol{\theta}}}$, we can derive that

$$\begin{aligned}\dot{V}_3&\le\frac{\theta_9}{\theta_{9\min}}\left(-K_1S_1^2\right)+S_1\theta_9P_{\mathrm{vds2}}-S_1\boldsymbol{\varphi}_{\mathrm{b}}^{\mathrm{T}}\tilde{\boldsymbol{\theta}}_{\mathrm{b}}\\&+\frac{\theta_{10}}{\theta_{10\min}}\left(-K_2S_2^2\right)+S_2\theta_{10}f_1I_{is2}-S_2\boldsymbol{\varphi}_{\mathrm{c}}^{\mathrm{T}}\tilde{\boldsymbol{\theta}}+\tilde{\boldsymbol{\theta}}^{\mathrm{T}}\boldsymbol{\Gamma}^{-1}\dot{\tilde{\boldsymbol{\theta}}}\\&\le\frac{\theta_9}{\theta_{9\min}}\left(-K_1S_1^2\right)+\frac{\theta_{10}}{\theta_{10\min}}\left(-K_2S_2^2\right)+S_1\theta_9P_{\mathrm{vds2}}\\&+S_2\theta_{10}f_1I_{is2}+\tilde{\boldsymbol{\theta}}^{\mathrm{T}}\left[\boldsymbol{\Gamma}^{-1}\mathrm{Proj}_{\hat{\boldsymbol{\theta}}}(\boldsymbol{\Gamma}\boldsymbol{\tau})-\boldsymbol{\tau}\right]\\&\le\frac{\theta_9}{\theta_{9\min}}\left(-K_1S_1^2\right)+\frac{\theta_{10}}{\theta_{10\min}}\left(-K_2S_2^2\right).\end{aligned} \tag{51}$$

Therefore, the asymptotical convergence of S_1 can be guaranteed by the proposed discontinuous projection-based ARC, and the asymptotical convergence of tracking error e will also be guaranteed, i.e. $e\to0$ as $t\to\infty$.

4 Experimental results

4.1 Experimental design

On the basis of the pneumatic bending actuator control system shown in Fig. 1, the following experiments were conducted with a sampling time of 0.005 s.

1. Three comparative control algorithms were employed:

C1: PID controller plus velocity and acceleration feedforward;

C2: Sliding mode controller (SMC);

C3: ARC designed in this study.

2. Two reference trajectories were chosen:

T1: point-to-point trajectory;

T2: [0, 0.5] Hz multi-sine trajectory.

4.2 Experimental results

The tracking results of the T1 and T2 trajectories are presented in Figs. 6 and 7, respectively. The SMC (C2) achieved good trajectory tracking performance, even without updating model parameters. For trajectory T1, the maximum dynamic tracking error of SMC (C2) was about 4.75°, and the maximum steady-state error was below 1.56°. Correspondingly, the maximum dynamic tracking error was about 5.27° for trajectory T2. Thus, the effectiveness of the proposed empirical nonlinear model and the modified flow rate model was verified. On the basis of the smooth SMC (C2), the ARC (C3) introduced parameter adaptation to reduce the model uncertainties. As a result, the ARC (C3) achieved the best performance for all trajectories compared with the PID controller plus velocity and acceleration feedforward (C1) and SMC (C2). For trajectory T1, the maximum dynamic tracking error of ARC (C3) was about 4.36°, and the maximum steady-state error was below 0.82°. Correspondingly, the maximum dynamic tracking error was about 3.67° for trajectory T2. Thus, the experimental results demonstrated the effectiveness of the modeling strategy and the high performance of the ARC method.

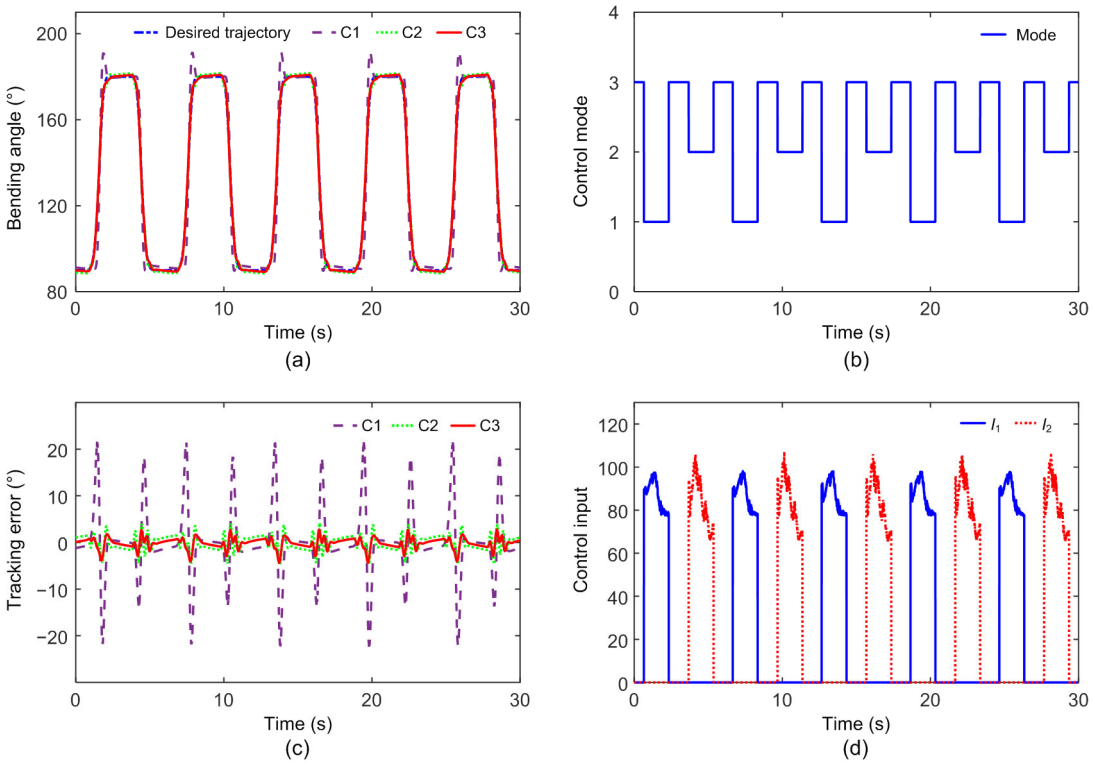

Fig. 6 Experimental results of T1 trajectory: (a) trajectory tracking results; (b) control modes of ARC (C3); (c) trajectory tracking errors; (d) control inputs of ARC (C3)

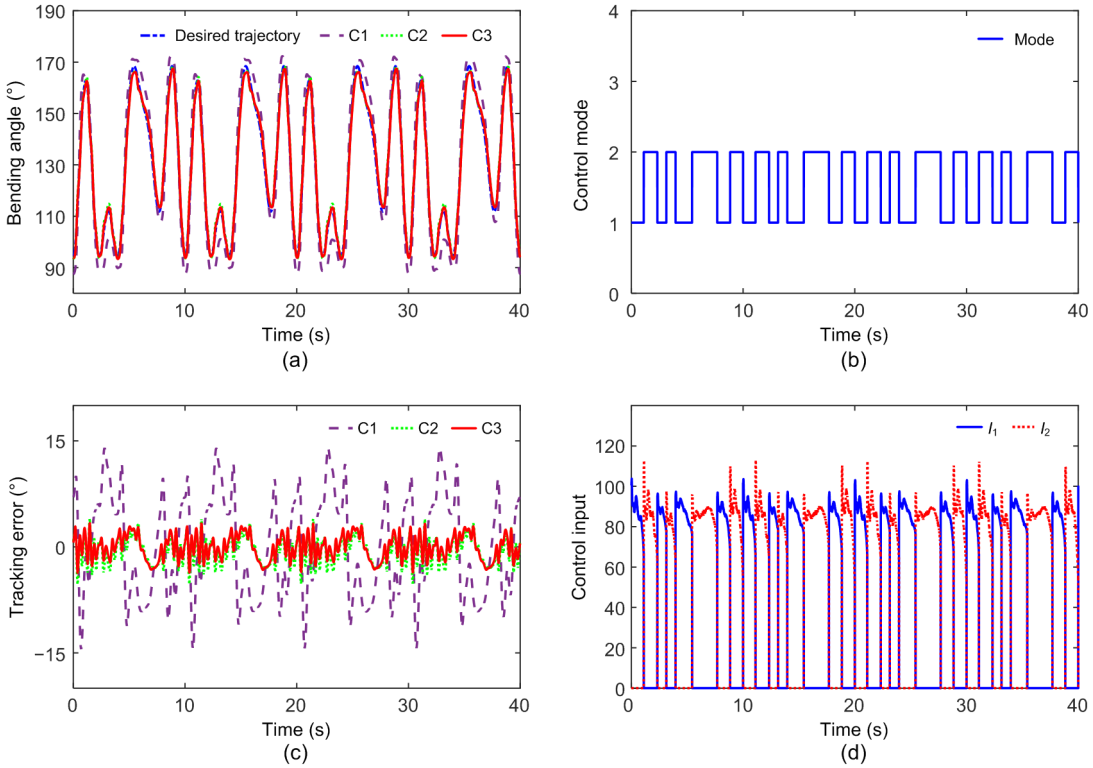

Fig. 7 Experimental results of T2 trajectory: (a) trajectory tracking results; (b) control modes of ARC (C3); (c) trajectory tracking errors; (d) control inputs of ARC (C3)

5 Conclusions

In this paper we proposed an empirical nonlinear model-based trajectory tracking control method for a pneumatic soft bending actuator. On the basis of a linear second-order transfer function model, a novel empirical nonlinear model was proposed and well-identified to improve the accuracy of the empirical FRSBA dynamic model. Moreover, a modified valve flow rate model was developed to accurately describe the mass flow rate of the unbalanced pneumatic proportional valve. Then, an adaptive robust control law was synthesized to govern and update the system with nonlinearities and uncertainties while ensuring satisfactory control performance. Finally, the results of comparative trajectory tracking experiments indicated the effectiveness of the modeling strategies and the validity of the proposed controller.

The empirical nonlinear model and the adaptive robust controller proposed in this study are able to govern the system with bounded uncertainties, and guarantee control performance. In actual application, large external disturbances (e.g. a large payload or external contact) are inevitable. In future work, position control under large but relatively deterministic disturbances will be researched.

Contributors

Cong CHEN and Jun ZOU designed the research, processed the data, wrote the first draft of this manuscript, and revised the final version. Jun ZOU provided funding support.

Conflict of interest

Cong CHEN and Jun ZOU declare that they have no conflict of interest.

References

Abbasi P, Nekoui MA, Zareinejad M, et al., 2020. Position and force control of a soft pneumatic actuator. *Soft Robotics*, 7(5):550-563. https://doi.org/10.1089/soro.2019.0065

Al-Ibadi A, Nefti-Meziani S, Davis S, 2018. Active soft end effectors for efficient grasping and safe handling. *IEEE Access*, 6:23591-23601. https://doi.org/10.1109/Access.2018.2829351

Bieze TM, Largilliere F, Kruszewski A, et al., 2018. Finite element method-based kinematics and closed-loop control of soft, continuum manipulators. *Soft Robotics*, 5(3):348-364. https://doi.org/10.1089/soro.2017.0079

Blumenschein LH, Gan LT, Fan JA, et al., 2018. A tip-extending soft robot enables reconfigurable and deployable antennas. *IEEE Robotics and Automation Letters*, 3(2):949-956. https://doi.org/10.1109/Lra.2018.2793303

Boyraz P, Runge G, Raatz A, 2018. An overview of novel actuators for soft robotics. *Actuators*, 7(3):48. https://doi.org/10.3390/act7030048

Bruder D, Gillespie B, Remy CD, et al., 2019. Modeling and control of soft robots using the Koopman operator and model predictive control. Proceedings of Robotics: Science and Systems.

Chen C, Tang W, Hu Y, et al., 2020. Fiber-reinforced soft bending actuator control utilizing on/off valves. *IEEE Robotics and Automation Letters*, 5(4):6732-6739. https://doi.org/10.1109/LRA.2020.3015189

Chen WB, Xiong CH, Liu CL, et al., 2019. Fabrication and dynamic modeling of bidirectional bending soft actuator integrated with optical waveguide curvature sensor. *Soft Robotics*, 6(4):495-506. https://doi.org/10.1089/soro.2018.0061

Deimel R, Brock O, 2013. A compliant hand based on a novel pneumatic actuator. Proceedings of the IEEE International Conference on Robotics and Automation, p.2047-2053. https://doi.org/10.1109/ICRA.2013.6630851

Deimel R, Radke M, Brock O, 2016. Mass control of pneumatic soft continuum actuators with commodity components. Proceedings of the IEEE/RSJ International Conference on Intelligent Robots and Systems, p.774-779. https://doi.org/10.1109/IROS.2016.7759139

Falkenhahn V, Hildebrandt A, Neumann R, et al., 2017. Dynamic control of the bionic handling assistant. *IEEE/ASME Transactions on Mechatronics*, 22(1):6-17. https://doi.org/10.1109/TMECH.2016.2605820

Fan JZ, Du QL, Yu QG, et al., 2020. Biologically inspired swimming robotic frog based on pneumatic soft actuators. *Bioinspiration & Biomimetics*, 15(4):046006. https://doi.org/10.1088/1748-3190/ab835a

Fang G, Wang XM, Wang K, et al., 2019. Vision-based online learning kinematic control for soft robots using local Gaussian process regression. *IEEE Robotics and Automation Letters*, 4(2):1194-1201. https://doi.org/10.1109/LRA.2019.2893691

Finnemore EJ, Franzini JB, 2002. Fluid Mechanics with Engineering Applications. McGraw-Hill, New York, USA, p.597.

Franco E, Garriga-Casanovas A, 2021. Energy-shaping control of soft continuum manipulators with in-plane disturbances. *The International Journal of Robotics Research*, 40(1):236-255. https://doi.org/10.1177/2F0278364920907679

Gerboni G, Diodato A, Ciuti G, et al., 2017. Feedback control of soft robot actuators via commercial flex bend sensors. *IEEE/ASME Transactions on Mechatronics*, 22(4):1881-

1888.
https://doi.org/10.1109/TMECH.2017.2699677

Hamidi A, Almubarak Y, Tadesse Y, 2019. Multidirectional 3D-printed functionally graded modular joint actuated by TCP FL muscles for soft robots. *Bio-Design and Manufacturing*, 2(4):256-268.
https://doi.org/10.1007/s42242-019-00055-6

Hyatt P, Kraus D, Sherrod V, et al., 2019a. Configuration estimation for accurate position control of large-scale soft robots. *IEEE/ASME Transactions on Mechatronics*, 24(1):88-99.
https://doi.org/10.1109/TMECH.2018.2878228

Hyatt P, Wingate D, Killpack MD, 2019b. Model-based control of soft actuators using learned non-linear discrete-time models. *Frontiers in Robotics and AI*, 6:22.
https://doi.org/10.3389/frobt.2019.00022

Ibrahim S, Krause JC, Raatz A, 2019. Linear and nonlinear low level control of a soft pneumatic actuator. Proceedings of the 2nd IEEE International Conference on Soft Robotics, p.434-440.
https://doi.org/10.1109/ROBOSOFT.2019.8722737

Jung J, Park M, Kim D, et al., 2020. Optically sensorized elastomer air chamber for proprioceptive sensing of soft pneumatic actuators. *IEEE Robotics and Automation Letters*, 5(2):2333-2340.
https://doi.org/10.1109/LRA.2020.2970984

Katzschmann RK, 2018. Building and Controlling Fluidically Actuated Soft Robots: from Open Loop to Model-based Control. PhD Thesis, Massachusetts Institute of Technology, Massachusetts, USA.

Khan AH, Li S, 2020. Sliding mode control with PID sliding surface for active vibration damping of pneumatically actuated soft robots. *IEEE Access*, 8:88793-88800.
https://doi.org/10.1109/Access.2020.2992997

Khan AH, Shao ZL, Li S, et al., 2020. Which is the best PID variant for pneumatic soft robots? An experimental study. *IEEE/CAA Journal of Automatica Sinica*, 7(2):451-460.
https://doi.org/10.1109/JAS.2020.1003045

Kim S, Laschi C, Trimmer B, 2013. Soft robotics: a bioinspired evolution in robotics. *Trends in Biotechnology*, 31(5):287-294.
https://doi.org/10.1016/j.tibtech.2013.03.002

Kwon J, Yoon SJ, Park YL, 2020. Flat inflatable artificial muscles with large stroke and adjustable force-length relations. *IEEE Transactions on Robotics*, 36(3):743-756.
https://doi.org/10.1109/TRO.2019.2961300

Laschi C, Mazzolai B, Cianchetti M, 2016. Soft robotics: technologies and systems pushing the boundaries of robot abilities. *Science Robotics*, 1(1):eaah3690.
https://doi.org/10.1126/scirobotics.aah3690

Li MH, Kang RJ, Branson DT, et al., 2018. Model-free control for continuum robots based on an adaptive Kalman filter. *IEEE/ASME Transactions on Mechatronics*, 23(1):286-297.
https://doi.org/10.1109/TMECH.2017.2775663

Liu S, Yao B, 2008. Coordinate control of energy saving programmable valves. *IEEE Transactions on Control Systems Technology*, 16(1):34-45.
https://doi.org/10.1109/TCST.2007.903073

Luo C, Wang K, Li GY, et al., 2019. Development of active soft robotic manipulators for stable grasping under slippery conditions. *IEEE Access*, 7:97604-97613.
https://doi.org/10.1109/Access.2019.2927354

Marchese AD, Tedrake R, Rus D, 2016. Dynamics and trajectory optimization for a soft spatial fluidic elastomer manipulator. *The International Journal of Robotics Research*, 35(8):1000-1019.
https://doi.org/10.1177/0278364915587926

Mohanty A, Yao B, 2011. Indirect adaptive robust control of hydraulic manipulators with accurate parameter estimates. *IEEE Transactions on Control Systems Technology*, 19(3):567-575.
https://doi.org/10.1109/TCST.2010.2048569

Müller D, Raisch A, Hildebrandt A, et al., 2020. Nonlinear model based dynamic control of pneumatic driven quasi continuum manipulators. Proceedings of the IEEE/SICE International Symposium on System Integration, p.277-282.
https://doi.org/10.1109/SII46433.2020.9026206

Pang W, Wang JB, Fei YQ, 2018. The structure, design, and closed-loop motion control of a differential drive soft robot. *Soft Robotics*, 5(1):71-80.
https://doi.org/10.1089/soro.2017.0042

Polygerinos P, Wang Z, Overvelde JTB, et al., 2015. Modeling of soft fiber-reinforced bending actuators. *IEEE Transactions on Robotics*, 31(3):778-789.
https://doi.org/10.1109/TRO.2015.2428504

Polygerinos P, Correll N, Morin SA, et al., 2017. Soft robotics: review of fluid-driven intrinsically soft devices; manufacturing, sensing, control, and applications in human-robot interaction. *Advanced Engineering Materials*, 19(12):1700016.
https://doi.org/10.1002/adem.201700016

Skorina EH, Luo M, Ozel S, et al., 2015. Feedforward augmented sliding mode motion control of antagonistic soft pneumatic actuators. Proceedings of the IEEE International Conference on Robotics and Automation, p.2544-2549.
https://doi.org/10.1109/ICRA.2015.7139540

Tang ZQ, Heung HL, Tong KY, et al., 2020. A probabilistic model-based online learning optimal control algorithm for soft pneumatic actuators. *IEEE Robotics and Automation Letters*, 5(2):1437-1444.
https://doi.org/10.1109/LRA.2020.2967293

Thuruthel TG, Ansari Y, Falotico E, et al., 2018. Control strategies for soft robotic manipulators: a survey. *Soft Robotics*, 5(2):149-163.
https://doi.org/10.1089/soro.2017.0007

Wang T, Zhang YC, Chen Z, 2018. Design and verification of

model-based nonlinear controller for fluidic soft actuators. Proceedings of the IEEE/ASME International Conference on Advanced Intelligent Mechatronics, p.1178-1183. https://doi.org/10.1109/AIM.2018.8452466

Xiang Z, 2010. Research on the Key Technologies of Pneumatic High-speed on-off Valve. PhD Thesis, Zhejiang University, Hangzhou, China (in Chinese).

Yang Y, Li Y, Chen Y, 2018. Principles and methods for stiffness modulation in soft robot design and development. *Bio-Design and Manufacturing*, 1(1):14-25. https://doi.org/10.1007/s42242-018-0001-6

Yao B, 1997. High performance adaptive robust control of nonlinear systems: a general framework and new schemes. Proceedings of the 36th IEEE Conference on Decision and Control, p.2489-2494. https://doi.org/10.1109/CDC.1997.657530

Yao B, Bu FP, Reedy J, et al., 2000. Adaptive robust motion control of single-rod hydraulic actuators: theory and experiments. *IEEE/ASME Transactions on Mechatronics*, 5(1):79-91. https://doi.org/10.1109/3516.828592

Zhang C, Zhu P, Lin Y, et al., 2021. Fluid-driven artificial muscles: bio-design, manufacturing, sensing, control, and applications. *Bio-Design and Manufacturing*, 4(1): 123-145. https://doi.org/10.1007/s42242-020-00099-z

Zhang J, Sheng J, O'Neill CT, et al., 2019. Robotic artificial muscles: current progress and future perspectives. *IEEE Transactions on Robotics*, 35(3):761-781. https://doi.org/10.1109/TRO.2019.2894371

Zhou JS, Chen XJ, Chang Y, et al., 2019. A soft-robotic approach to anthropomorphic robotic hand dexterity. *IEEE Access*, 7:101483-101495. https://doi.org/10.1109/Access.2019.2929690